A three-dimensional numerical simulation of the transport phenomena in the cathodic side of a PEMFC

J.J. HWANG[1,*], C.K. CHEN[2], R.F. SAVINELL[3], C.C. LIU[3] and J. WAINRIGHT[3]

[1]*Institute of Advanced Science and Technology, Mingdao University, Changhua, 523 Taiwan, ROC*
[2]*Department of Mechanical Engineering, National Cheng-Kung University, Tainan 701, Taiwan, ROC*
[3]*Department of Chemical Engineering, Case Western Reserve University, Cleveland, 44106 OH, USA*
(*author for correspondence, e-mail: azaijj@mdu.edu.tw)*

Abstract

A three-dimensional numerical model is developed to simulate the transport phenomena on the cathodic side of a polymer electrolyte membrane fuel cell (PEMFC) that is in contact with parallel and interdigitated gas distributors. The computational domain consists of a flow channel together with a gas diffusion layer on the cathode of a PEMFC. The effective diffusivities according to the Bruggman correlation and Darcy's law for porous media are used for the gas diffusion layer. In addition, the Tafel equation is used to describe the oxygen reduction reaction (ORR) on the catalyst layer surface. Three-dimensional transport equations for the channel flow and the gas diffusion layer are solved numerically using a finite-volume-based numerical technique. The nature of the multi-dimensional transport in the cathode side of a PEMFC is illustrated by the fluid flow, mass fraction and current density distribution. The interdigitated gas distributor gives a higher average current density on the catalyst layer surface than that with the parallel gas distributor under the same mass flow rate and cathode overpotential. Moreover, the limiting current density increased by 40% by using the interdigitated flow field design instead of the parallel one.

List of symbols

c_o oxygen concentration (mol m^{-3})
C_o normalized oxygen concentration, c_o/c_{ref}
c_{ref} reference oxygen concentration (mol m^{-3})
c_w water vapor concentration (mol m^{-3})
C_w normalized water vapor concentration, c_w/c_{ref}
D_o binary diffusivity of oxygen in the air (m^2 s^{-1})
$D_{o, eff}$ effective diffusivity of oxygen in the gas diffusion layer (m^2 s^{-1})
D_w binary diffusivity of water vapor in the air (m^2 s^{-1})
$D_{w, eff}$ effective diffusivity of water vapor in the gas diffusion layer (m^2 s^{-1})
F Faraday's constant (96 487 C mol^{-1})
H height of the computation module, Figure 2 (m)
H_1 channel height, Figure 2 (m)
H_2 thickness of the diffusion layer, Figure 2 (m)
I averaged current density (A m^{-2})
i local current density (A m^{-2})
i_o exchange current density (A m^{-2})
K permeability of the porous medium (m^2)
L length of the computational domain (m)
$\dot{m}$ mass flux (kg m^{-2} s^{-1})
n number of electron transfer during the ORR

p pressure (Pa)
p_{in} inlet pressure (Pa)
p_{out} outlet pressure (Pa)
R universal gas constant (W mol^{-1} K^{-1})
R_Ω ohmic resistance of the fuel cell (Ω m^2)
T temperature (K)
u, v, w velocity components in the x, y, and z directions, respectively (m s^{-1})
V_{oc} open circuit voltage (V)
V_{cell} cell voltage (V)
W width of the computational domain, Figure 2 (m)
W_1 half width of the flow channel, Figure 2 (m)
W_2 width of the shoulder of the gas distributor, Figure 2 (m)
x, y, z coordinate system, Figure 1 (m)
X nondimensional x coordinate, x/L

Greek symbols

α net water transport coefficient through the membrane into the cathode
ε porosity of the gas diffusion layer
ρ density (kg m^{-3})
η cathodic overpotential (V)
τ tortuosity of the porous gas diffusion layer

1. Introduction

The polymer electrolyte membrane fuel cell (PEMFC) has been considered as an alternative power source for various applications. The requirements of compactness, high power density, performance, stability, and low cost lead to the optimization of different aspects of a PEMFC. A meaningful theoretical analysis of the critical aspects of a PEMFC is essential for the optimization of the fuel cell itself. Mathematical modelings of a PEMFC [1–6] have been proposed to determine the cell voltage as a function of the current density under various operating conditions. Due to the complex interaction of electrochemical reaction, hydrodynamics, and multi-component transport in the fuel cell, however, fundamental transport phenomena of a PEMFC still require further investigation.

For the performance of a PEMFC, the cathode is considered the dominant component. This is due to the slow kinetics of oxygen reduction [7] and the cell performance depends strongly on the oxygen transport rate to the cathode. Therefore, modeling of the cathodic half cell of a PEMFC has been emphasized [7–16]. Kulikovsky et al. [8] numerically simulated the cathodic compartment of a PEMFC and investigated the influence of the two-dimensional effects on the cathode performance. The low diffusivity in the backing layer created dead zones in front of the current collector where catalysts were not used and could be removed from these zones for cost-reduction purposes. Yi and Nguyen [9] proposed a two-dimensional multi-component transport model to investigate the gas hydrodynamics in a PEMFC cathode with an interdigitated gas distributor. The flow patterns and the distributions of gaseous species in the porous cathode were presented at a fixed cathodic overpotential value of $\eta = 0.3$. The average current density decreased with an increase in the electrode thickness and the shoulder width when both the pressure drop across the module and the cathodic overpotential were kept constant. Kazim et al. [10] developed a two-dimensional numerical model for the cathode of a PEMFC with both interdigitated and parallel flow fields. They showed that the interdigitated gas distributor was effective in enhancing the transport rate of the reactive gases to the active sites in the cathode. Gurau et al. [11] proposed a one-dimensional mathematical model of a PEMFC containing a cathode gas channel, a gas diffusion layer, a catalyst layer, and a membrane. Analytical solutions were derived for the coupled equations, consisting of the oxygen mass transport equation and Ohm's law for proton migration in a heterogeneous domain. Wang et al. [12] presented a two-dimensional numerical study of two-phase flow transport in the air cathode of a PEMFC. Their model encompassed both single- and two-phase regimes corresponding to low and high current densities and was capable of predicting the transition between the two regimes.

In contrast to the above one-dimensional or two-dimensional models for the cathodic half cell of a PEMFC, the objective of this work is to develop a three-dimensional numerical model to simulate the transport phenomena in the cathode of a PEMFC. Emphasis is placed on the effects of the cathodic overpotential and the flow-distributor geometry on the electrochemical performance of the fuel cell. Fluid flow, concentration of gaseous species and current density distributions are presented to illustrate the relationship between the fluid-flow and the electrochemical characteristics in the cathode of a PEMFC. Polarization characteristics for parallel and interdigitated flow fields are simulated and compared. The results obtained provide an insight into the multi-dimensional transport phenomena in the cathode, which will be helpful in the design and optimization of a PEMFC.

2. Numerical model

Figure 1(a) and (b) show the schematic drawings of the cathode of a PEMFC in contact with parallel and interdigitated gas distributors, respectively. In the parallel flow field, the oxygen enters the gas distributor and then traverses an array of parallel channels equally spaced by the current collectors. For the interdigitated flow field, the inlet and outlet channels are dead-ended downstream and upstream, respectively. In this circumstance, the oxygen flows across the porous gas diffusion layer from the inlet channel to the outlet channel. Figure 2 is a sectional yz plane view of the interdigitated flow field, in which the oxygen is supplied to the inlet channel, passes through the gas diffusion layer above the current collectors, and then exits from the outlet channel. The ORR occurs at the catalyst layer surface ($y = H$). Detailed dimensions of the present computation module are given in Table 1.

2.1. *Governing equations*

The following assumptions are used in this study: (1) the gas mixtures are ideal gas, incompressible and laminar flow, (2) the gas diffusion layer is homogeneous and isotropic with uniform morphological properties such as porosity, tortuosity and permeability, (3) the fuel cell operates at a constant temperature, (4) water in the electrode exits as vapor only, and (5) the catalyst layer is treated as an ultra-thin layer; thus the ORR is considered to occur only at the surface of the catalyst layer.
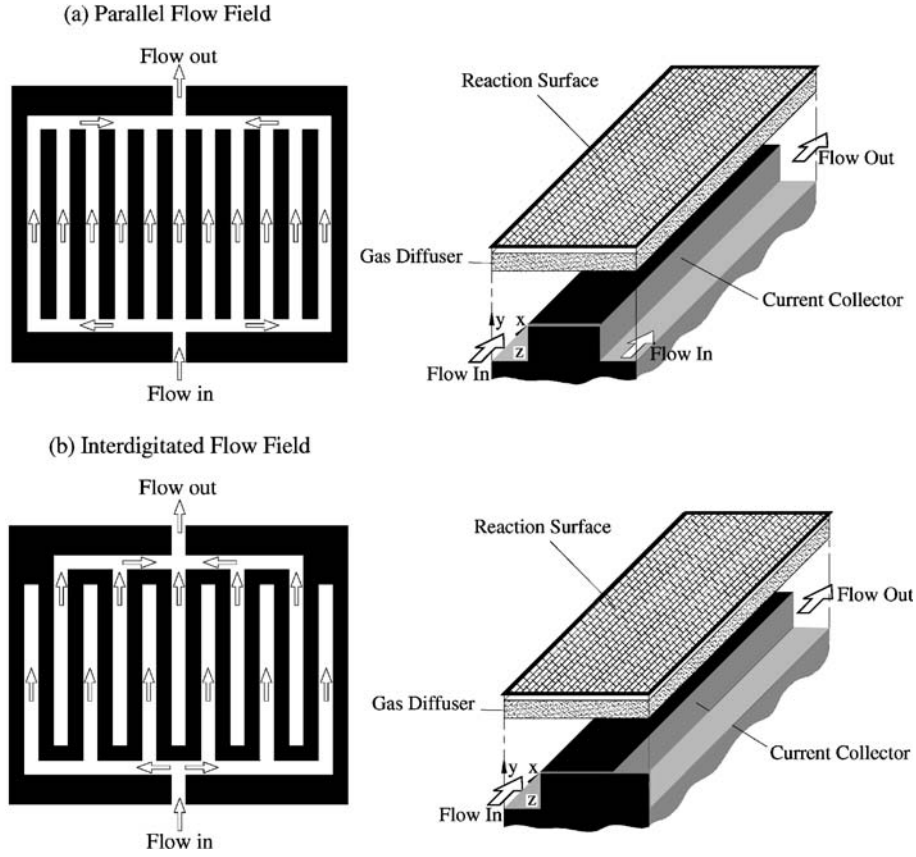
Fig. 1. Geometries and coordinate systems of the parallel and interdigitated flow fields.
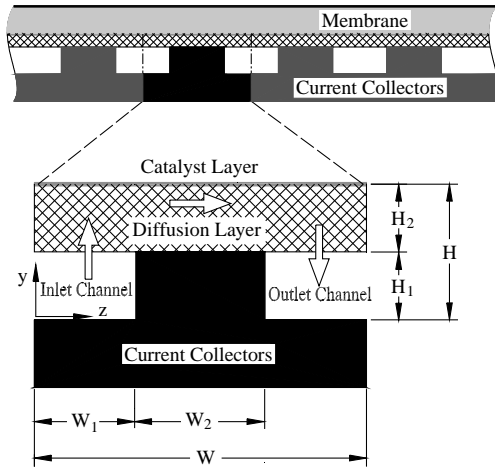

Fig. 2. Sectional view of the interdigitated flow field.

Table 1. Geometric and physical parameters used in the present simulation

Quantity	Value	Reference
Domain length, L	10 mm	Assumed
Domain height, H	0.7 mm	Assumed
Domain width, W	2.0 mm	Assumed
Flow channel height, H_1	0.5 mm	Assumed
Diffusion layer thickness, H_2	0.2 mm	Assumed
Flow channel width, $2W_1$	1.0 mm	Assumed
Shoulder (current collector) width, W_2	1.0 mm	Assumed
Faraday constant, F	96 487 C mol^{-1}	–
Permeability of backing layer, K	1.0×10^{-12} m^2	[10]
Universal gas constant, R	8.314 J mol^{-1} K^{-1}	–
Open circuit voltage, V_{oc}	1.1 V	[9, 10]
Net water transport coefficient, α	0.1	[9]
Backing layer porosity (void fraction), ε	0.3	[9]
Tortuosity of the diffusion layer, τ	1.5	[9]
O$_2$ stoichiometric flow ratio at $I = 1$ A /cm^{-2}	3.0	–
Relative humidity of inlet oxygen	0%	–
Exchange current density, i_0	100 A m^{-2}	[7]
Reference oxygen concentration, c_{ref}	35.7 mol m^{-3}	[9]

Under these assumptions, the three-dimensional equations for gas channel and gas diffusion layer for the interdigitated and parallel flow fields can be written as

$$\frac{\partial \rho u}{\partial x} + \frac{\partial \rho v}{\partial y} + \frac{\partial \rho w}{\partial z} = 0 \tag{1}$$

$$\rho u \frac{\partial u}{\partial x} + \rho v \frac{\partial u}{\partial y} + \rho w \frac{\partial u}{\partial z} = -\varepsilon \frac{\partial p}{\partial x} + \mu \left(\frac{\partial^2 u}{\partial x^2} + \frac{\partial^2 u}{\partial y^2} + \frac{\partial^2 u}{\partial z^2} \right) - \frac{\mu}{K} \varepsilon u \tag{2}$$

$$\rho u \frac{\partial v}{\partial x} + \rho v \frac{\partial v}{\partial y} + \rho w \frac{\partial v}{\partial z} = -\varepsilon \frac{\partial p}{\partial y} + \mu \left(\frac{\partial^2 v}{\partial x^2} + \frac{\partial^2 v}{\partial y^2} + \frac{\partial^2 v}{\partial z^2} \right) - \frac{\mu}{K} \varepsilon v \tag{3}$$

$$\rho u \frac{\partial w}{\partial x} + \rho v \frac{\partial w}{\partial y} + \rho w \frac{\partial w}{\partial z} = -\varepsilon \frac{\partial p}{\partial z} + \mu \left(\frac{\partial^2 w}{\partial x^2} + \frac{\partial^2 w}{\partial y^2} + \frac{\partial^2 w}{\partial z^2} \right) - \frac{\mu}{K} \varepsilon w \tag{4}$$

$$\rho u \frac{\partial c_o}{\partial x} + \rho v \frac{\partial c_o}{\partial y} + \rho w \frac{\partial c_o}{\partial z} = \rho D_{o,eff}\left(\frac{\partial^2 c_o}{\partial x^2} + \frac{\partial^2 c_o}{\partial y^2} + \frac{\partial^2 c_o}{\partial z^2}\right) \tag{5}$$

$$\rho u \frac{\partial c_w}{\partial x} + \rho v \frac{\partial c_w}{\partial y} + \rho w \frac{\partial c_w}{\partial z} = \rho D_{w,eff}\left(\frac{\partial^2 c_w}{\partial x^2} + \frac{\partial^2 c_w}{\partial y^2} + \frac{\partial^2 c_w}{\partial z^2}\right) \tag{6}$$

where u, v, and w, are the intrinsic fluid velocities in three directions, respectively. The other terms are defined as shown in the list of symbols. Both $D_{o,eff}$ and $D_{w,eff}$ are modified by Bruggman correlation [13] in order to account for the effects of porosity and tortuosity (τ) in the porous electrode, i.e.,

$$D_{o,eff} = \varepsilon^\tau D_o \tag{7}$$

$$D_{w,eff} = \varepsilon^\tau D_w \tag{8}$$

In general, the momentum equations are valid for both the porous gas diffusion layer and the open flow channel. They are reduced to the extended Darcy's law for flow in the porous cathode with a small permeability [3, 14], and become the Navier–Stokes equations inside the flow channel with the porosity being unity and the permeability being infinite.

2.2. Boundary conditions

The boundary conditions of the present computational domain can be summarized as

(i) At the oxygen inlet ($x=0$, $0 \leqslant y \leqslant H_1$, $0 \leqslant z \leqslant W_1$; $x=0$, $H_1 \leqslant y \leqslant H$, $0 \leqslant z \leqslant W$ for interdigitated flow distributor), ($x=0$, $0 \leqslant y \leqslant H_1$, $0 \leqslant z \leqslant W_1$; $x=0$, $0 \leqslant y \leqslant H_1$, $W_1 + W_2 \leqslant z \leqslant W$; $x=0$, $H_1 \leqslant y \leqslant H$, $0 \leqslant z \leqslant W$ for parallel flow distributor)

$$p = p_{in}, c_o = c_{o,in}, c_w = c_{w,in} \tag{9}$$

(ii) At the current collector surfaces ($0 \leqslant x \leqslant L$, $y=0, 0 \leqslant z \leqslant W_1; 0 \leqslant x \leqslant L, y=0, W_1 + W_2 \leqslant z \leqslant W$; $0 \leqslant x \leqslant L$, $y=H_1$, $W_1 \leqslant z \leqslant W_1 + W_2$; $0 \leqslant x \leqslant L$, $0 \leqslant y \leqslant H_1$, $z=W_1$; $0 \leqslant x \leqslant L, 0 \leqslant y \leqslant H_1, z=W_2$)

$$u = v = w = 0, \frac{\partial c_o}{\partial y} = \frac{\partial c_w}{\partial y} = \frac{\partial p}{\partial y} = 0 \tag{10}$$

(iii) At the symmetry planes ($0 < x < L, 0 \leqslant y \leqslant H$, $z=0$ and W)

$$\frac{\partial u}{\partial z} = \frac{\partial v}{\partial z} = \frac{\partial w}{\partial z} = \frac{\partial c_o}{\partial z} = \frac{\partial c_w}{\partial z} = \frac{\partial p}{\partial z} = 0 \tag{11}$$

(iv) At the module outlet ($x=L$, $0 \leqslant y \leqslant H_1$, $W_1 + W_2 \leqslant z \leqslant W$; $x=L$, $H_1 \leqslant y \leqslant H$, $0 \leqslant z \leqslant W$ for interdigitated flow distributor), ($x=L$, $0 \leqslant y \leqslant H_1$, $0 \leqslant z \leqslant W_1$; $x=L$, $0 \leqslant y \leqslant H_1$, $W_1 + W_2 \leqslant z \leqslant W$; $x=L$, $H_1 \leqslant y \leqslant H$, $0 \leqslant z \leqslant W$ for parallel flow distributor)

$$p = p_e, \frac{\partial c_o}{\partial x} = \frac{\partial c_w}{\partial x} = 0 \tag{12}$$

(v) At the active surface for the ORR ($0 \leqslant x \leqslant L$, $y = H$, $0 \leqslant z \leqslant W$)

$$u = v = w = 0, \frac{\partial p}{\partial y} = 0, D_{o,eff}\frac{\partial c_o}{\partial y} - \frac{i}{nF} = 0 \quad and$$

$$D_{w,eff}\frac{\partial c_w}{\partial y} + \frac{2(1 + 2\alpha)i}{nF} = 0 \tag{13}$$

The rate of electrochemical reaction in the catalyst layer can be determined using the Tafel equation to describe the relationship of the local current density and oxygen concentration

$$i = i_0 \frac{c_o}{c_{ref}} \exp\left(\frac{2F}{RT}\eta\right) \tag{14}$$

Therefore, the boundary conditions for the oxygen and water vapor concentrations at the reaction surface become, respectively

$$D_{o,eff}\frac{\partial c_o}{\partial y} + \left[\frac{i_0}{nFc_{ref}}\exp\left(\frac{2F}{RT}\eta\right)\right]c_o = 0 \tag{15}$$

$$D_{w,eff}\frac{\partial c_w}{\partial y} - \left[\frac{2(1 + 2\alpha)i_0}{nFc_{ref}}\exp\left(\frac{2F}{RT}\eta\right)\right]c_o = 0 \tag{16}$$

In this study, the cathodic overpotential η is varied to determine the corresponding oxygen and vapor concentrations. Once the oxygen concentration in the gas diffusion layer is determined, the local current density generated at the reaction surface is calculated using the following equation:

$$i(x,z) = nFD_{o,eff}\frac{\partial c_o}{\partial y}\bigg|_{y=H} \tag{17}$$

The averaged current density on the ORR surface is then determined by

$$I = \frac{1}{W \times L}\int_0^W\int_0^L i(x,z)\mathrm{d}x\mathrm{d}z \tag{18}$$

2.3. Numerical procedures

The governing equations are numerically solved by the control-volume-based finite difference method [15]. The discretization procedure ensures the conservation of mass, momentum, and concentration over each control

volume. Three momentum equations corresponding to three coordinates are solved, followed by a pressure correction equation for the mass balance. Concentration transport equations are solved after the bulk flow calculation. Velocity control volumes are staggered with respect to the main control volumes, and coupling of the pressure and velocity fields is treated via the SIMPLER pressure correction algorithm [16, 17]. The upwind difference scheme is used to treat the diffusion and convective terms. Because of the large variations in the source terms, under-relaxation is necessary for the dependent variables and the source terms to achieve convergence. Line inversion iteration with typical under-relaxation values of 0.1 for the velocity term and pressure correction terms is incorporated to the facilitated calculation. Solutions are considered to be converged at each test condition after the ratio of residual source (including mass, momentum, and species) to the maximum flux across a control surface becomes below 1.0×10^{-6}.

Computations were performed on $60 \times 20 \times 20$ (X by Y by Z) straight-line grids in this work. Additional runs for the coarser meshes, $40 \times 12 \times 12$, and the finer meshes, $70 \times 30 \times 30$, were used to asses the grid independence. A comparison of the results of the two grid sizes, $60 \times 20 \times 20$, and $70 \times 30 \times 30$, shows that the maximum discrepancies in the axial velocity and oxygen concentration profiles are 1.5 and 1.6%, respectively. In addition, computation results indicate a maximum change of 2.1% in current density distribution between the solutions of $60 \times 20 \times 20$, and $70 \times 30 \times 30$ grids. These changes are small and the accuracy of the solutions on a $60 \times 20 \times 20$ grids is deemed satisfactory. A typical simulation requires about 500 min of central processing unit time on a Pentium III 700 MHz PC.
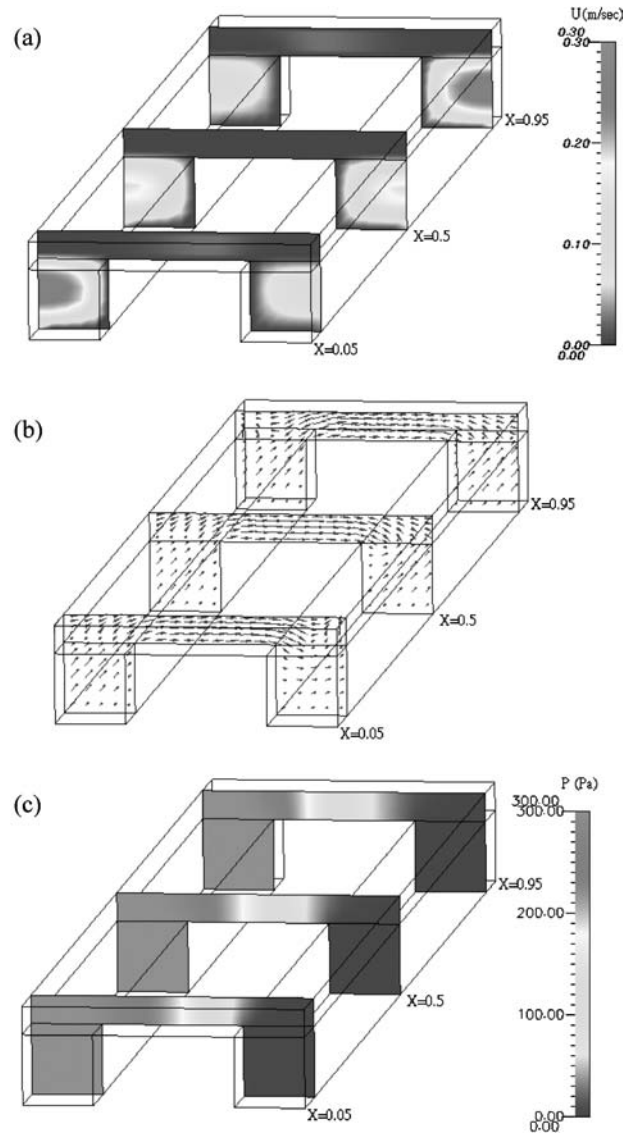

Fig. 3. Fluid flow structures in the channel and gas diffusion layer at several axial stations of the interdigitated flow field, (a) axial velocities (u), (b) secondary-flow vectors (composed by v and w), and (c) static pressure distributions at $\eta = 0.145$ V.

3. Results and discussion

3.1. Flow structures

The transport phenomena in the flow channel, as well as in the gas diffusion layer of a fuel cell, are important. Figure 3 shows the development of fluid flow in an interdigitated gas distributor, including the axial flow velocities (u), secondary flow vectors (composed by v and w), and static pressure distributions. The results at three nondimensional axial stations, i.e., $X = 0.05$, 0.5, and 0.95, are presented under a fixed cathodic overpotential of $\eta = 0.145$ V. Figure 3(a) shows that the axial velocity is higher at the central core of the flow channel and reduces essentially to zero in the gas diffusion layer because of significant surface drag in the porous medium. In addition, due to the dead-end of the inlet channel, the axial velocity gradually decreases along the axial direction. In contrast, the axial velocity increases along the distance of the outlet channel because the fluid from the inlet channel flows across the gas diffusion layer and successively infuses into the mainstream of the outlet channel. This phenomenon can be seen in Figure 3(b), which shows that the secondary-flow vectors in the gas diffusion layer directing the stream from the inlet channel to the outlet channel. This forced convection mechanism in the diffusion layer enhances the mass transport near the reaction surface and thus promotes the cell performance, which will be shown later. Figure 3(c) shows the static pressure distribution in the flow channel and gas diffusion layer. The pressure distributions both in the inlet and the outlet channel are relatively uniform and can be considered as constant pressure chambers. Significant pressure gradients are observed for flow across the diffusion layer above the current collectors.

3.2. Concentration distribution

Figure 4 shows the typical oxygen and water vapor concentration distributions at several axial stations of the interdigitated flow field. In this figure, the cathodic overpotential is fixed at $\eta = 0.173$ V and the scalar beside the color legend represents the normalized concentration, i.e., $C_o = c_o/c_{ref}$, and $C_w = c_w/c_{ref}$. The oxygen concentration in the flow field is closely related to the flow evolution shown in Figure 3. The oxygen concentration in the inlet channel decreases slightly along the axial distance (x). A significant variation of the oxygen concentration is found in the diffusion layer, especially near the reaction surface ($y = H$). At a fixed axial station, i.e. $X = 0.5$, the oxygen concentration in the diffusion layer decreases from the inlet channel, approaches a minimum value, and increases slightly thereafter. The lowest values of C_o are in the region where the flow turns into the outlet channel (Figure 3(b)), i.e., at about $z = W_1 + W_2$ near the reaction surface. By comparison, two-dimensional simulations [10, 11] showed that the oxygen concentration decreases monotonically along the z direction as the flow passes through the gas diffusion layer, and the minimum C_o is at the mid-plane of the outlet channel, i.e., $z = W$. This discrepancy in oxygen concentration distribution between our three-dimensional and the previous two-

dimensional simulation may be explained as follows. In the 3-D simulation, the core of outlet channel has a higher oxygen concentration than the corresponding diffusion layer. This is due to the oxygen accumulation from the outlet channel upstream where the oxygen passing through the diffusion layer is not consumed completely by the cathode reaction. Thus, oxygen diffuses into the gas diffusion layer from the outlet channel. The compromise of the forward forced convection (Figure 3(b)) and the backward diffusion, described above, results in a local minimum C_o at about $z = W_1 + W_2$. This diffusion mechanism cannot be predicted in the two-dimensional simulation. In the two-dimensional model, the oxygen flux at the interface of the gas diffusion layer and outlet channel is set to be zero as a boundary condition of the module, and there is no oxygen diffusion from the outlet channel into the gas diffusion layer.

As for C_w distribution, it increases along the flow direction due to the convective accumulation downstream of the vapor generated on the ORR surfaces. Note that the water vapor concentration in the inlet channel is not zero, but is relatively small for these conditions. This is an important result – a high concentration of water in the inlet channel can lead to condensation. Given that the inlet channel is dead-ended, condensation in the inlet channel could lead to irreversible build-up of liquid water and eventual cell failure.

Figure 5 shows the effect of cathodic overpotential on the oxygen concentration in the interdigitated flow field. The cathodic overpotential is varied from $\eta = 0.162$–0.234 V. The oxygen concentration changes slightly between the entrance and the exit of the module at the smallest η. However, the oxygen consumption is significant for high values of η due to the increased rate of reaction. Note that at $\eta = 0.234$ V, the oxygen near the catalyst layer surface is nearly depleted, meaning that the reaction has approached a limiting current density.

3.3. Gas distributor geometry effect

Figure 6 compares the oxygen concentration distribution at the mid-plane of the channel ($X = 0.5$) between the interdigitated and parallel gas distributors. In this figure, the two gas distributors have the same mass flux, $\dot{m} = 0.078$ kg m^{-2} s^{-1}, and the cathodic overpotential, $\eta = 0.198$ V. As shown in Figure 6(b), the parallel flow field has a symmetric oxygen concentration profile, while the oxygen concentration in the inlet channel is higher than that in the outlet channel for the interdigitated flow field. In general, for the parallel flow field, oxygen in the channel flow transfers the oxygen laterally into the backing layer via diffusion. The oxygen concentration in the diffusion layer above the current collector is small, indicating that the catalysts are not used effectively. In contrast, the oxygen concentration near the reaction surface is relatively uniform for the interdigitated flow field (Figure 6(a)) because the forced

(a) Oxygen concentration distribution
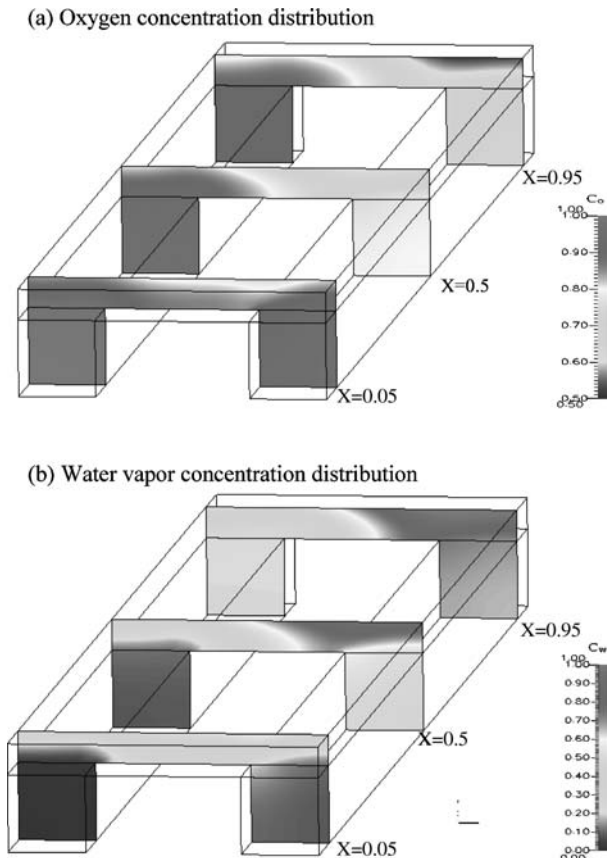
(b) Water vapor concentration distribution

Fig. 4. (a) Oxygen concentration and (b) water vapor concentration distributions in the channel flow and gas diffusion layer at several axial stations of the interdigitated flow field for $\eta = 0.173$ V.
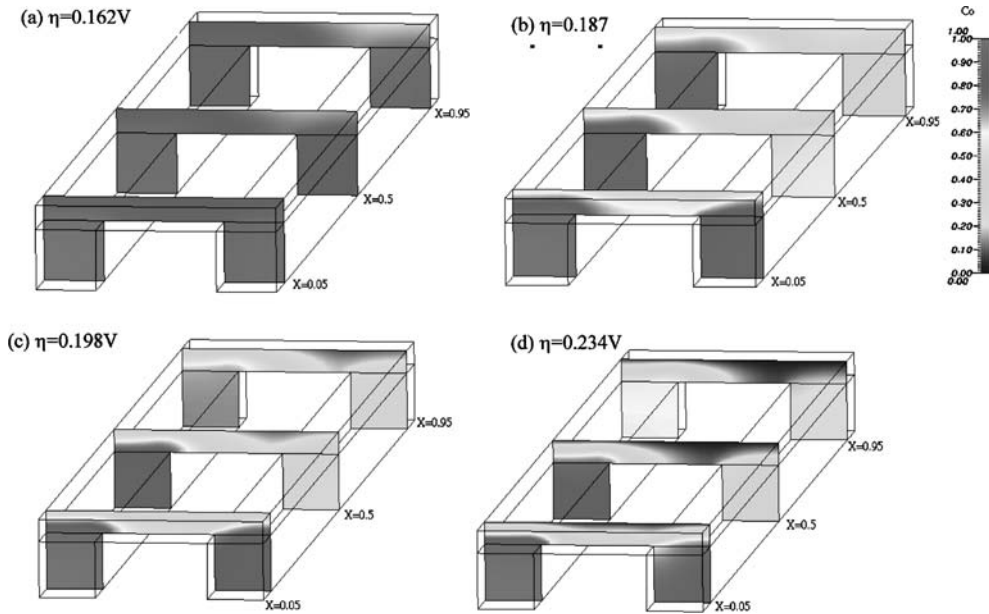
Fig. 5. Effect of cathodic overpotential on the oxygen concentration distribution at several axial stations of the channel. (a) $\eta = 0.162$ V, (b) $\eta = 0.187$ V, (c) $\eta = 0.198$ V, and (d) $\eta = 0.234$ V.

convection in the diffusion layer (Figure 3(b)) permits more oxygen to diffuse, enhancing the chemical reaction on the catalyst layer surface.

Figure 7 shows the current density distribution on the ORR surface for various cathodic overpotentials and gas distributors. At a fixed value of η, the region adjacent to the entrance of the gas distributor shows a large local current density because of the incoming fresh oxygen reacted on the catalyst surface. In addition, the current density on the ORR surface above the inlet channel is higher than that above the outlet channel. Figure 7(b) and (c) compare the current density distribution on the catalyst layer surface between the interdigitated and parallel flow fields at a fixed cathodic overpotential of $\eta = 0.198$ V. The local current densities on the catalyst layer surface of the interdigitated flow field are higher than those of the parallel flow field. The

interdigitated flow field result shows that the local minima of the current-density distribution is at about $z = W_1 + W_2$, consistent with the location of lowest oxygen concentration shown in Figure 4. This characteristic of the current-density distribution was not predicted in the two-dimensional model. For the parallel flow field shown in Figure 7(c), there is almost no current density generated from the catalyst layer surface above the center of the current collector, except in the entrance region. The parallel flow field cannot provide a high oxygen transfer rate to this region because of the diffusion limitations, whereas an interdigitated flow field can supply oxygen at a much higher rate by forced convection.
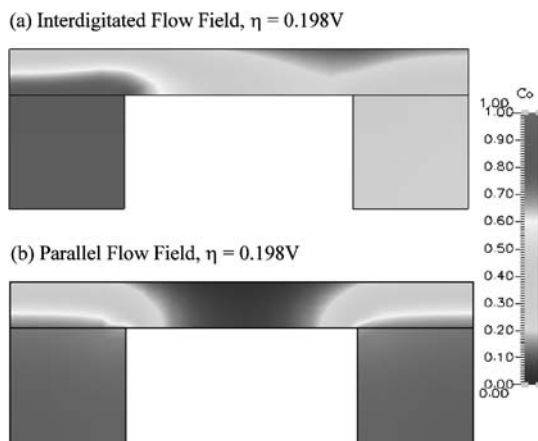

Fig. 6. Effect of the gas-distributor geometry on the oxygen concentration distribution at the mid-plane ($X = 0.5$) of the flow channel.
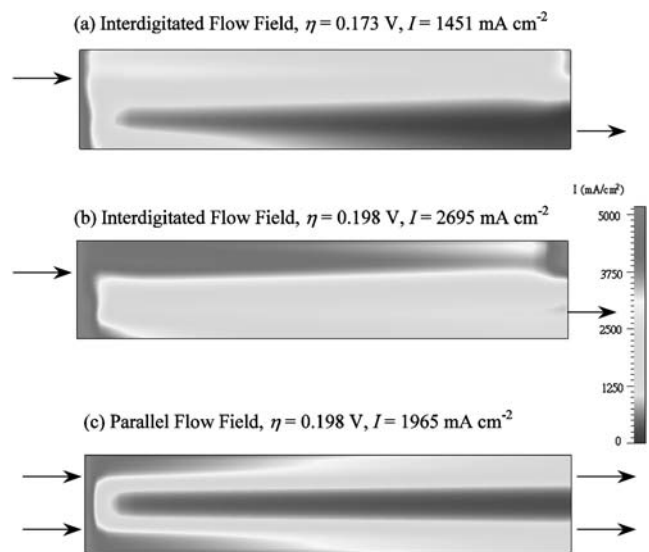

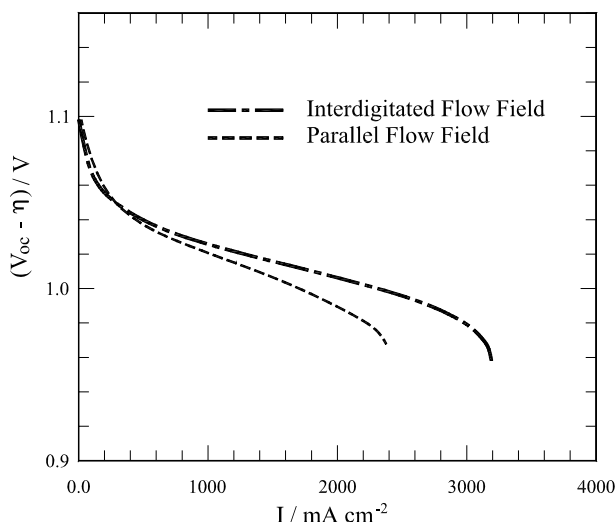Fig. 7. Current density distributions on the ORR surface for different overpotentials and gas distributors.

Fig. 8. Comparison of polarization curve between the interdigitated flow field and parallel flow field.

3.4. *Polarization curve*

The polarization characteristics of a fuel cell are a convenient means to evaluate the performance of a fuel cell with various flow field plates. Figure 8 shows a typical set of polarization curves, where the abscissa is the average current density generated from the reaction surface and the ordinate is the open circuit potential (V_{oc}) minus the cathodic overpotential. At low current density, the oxygen diffuses into the parallel gas diffusion layer and provides sufficient oxygen for the reaction on the ORR surface. Thus, the performance of the fuel cells with either the parallel or the interdigitated gas distributors are relatively similar. Nevertheless, the parallel gas distributor performs slightly better than the interdigitated gas distributor for $I < 300$ mA cm^{-2}. However, at high current densities, say $I > 1000$ mA cm^{-2}, the interdigitated flow field obviously performs better than the parallel one. In addition, the limiting current density for the interdigitated flow field is about 40% higher than that for the parallel flow field. This shows again that the interdigitated gas distributors converting the transport of the reactant gas to the catalyst-layer surface from a diffusion mechanism to a forced convection mechanism has significantly improved the performance of the PEMFC.

4. Conclusions

A three-dimensional computational model has been developed to study the transport phenomena in a PEMFC cathode attached to two types of gas distributors; interdigitated and parallel. Darcy's law together with effective diffusivities modified by the Bruggman equation are employed to describe the gas transport in the porous electrode, and the Tafel equation is used to relate the oxygen concentration and the current density

to the overpotential on the reaction surface. The effects of gas-distributor geometry and cathodic overpotential on the oxygen transport are illustrated by the flow structure, oxygen concentration and current density distributions. The distribution of local current density on the catalyst-layer surface has been predicted with the present three-dimensional model, with noticeable differences to previous two-dimensional predictions. It is shown that the interdigitated gas distributor converts the transport of oxygen to the catalyst layer surface from a diffusion mechanism to a forced convection mechanism. This improves the cell performance and also enhances the limiting current density.

References

1. S. Srinivasan, D.J. Mankoo, H. Koch and M.A. Enayetullah, *J. Power Sources* **29** (1988) 367.
2. T.E. Springer, T.A. Zawodinski and S. Gottesfeld, *J. Electrochem. Soc.* **136** (1991) 2334.
3. D.M. Bernardi and M.W. Verbrugge, *J. Electrochem. Soc.* **139** (1992) 2477.
4. T.E. Springer, M.S. Wilson and S. Gottesfeld, *J. Electrochem. Soc.* **140** (1993) 3513.
5. Y.W. Rho, S. Srinivasan and Y.T. Kho, *J. Electrochem. Soc.* **141** (1994) 2089.
6. K. Broka and P. Ekdunge, *J. App. Electrochem.* **27** (1997) 281.
7. T.E. Springer, T.A. Zawodinski and S. Gottesfeld, *J. Electrochem. Soc.* **138** (1991) 587.
8. A.A. Kulikovsky, J. Divisek and A.A. Kornyshev, *J. Electrochem. Soc.* **146** (1999) 3981.
9. J.S. Yi and T.V. Nguyen, *J. Electrochem. Soc.* **146** (1999) 38.
10. A. Kazim, H.T. Liu and P. Forges, *J. Appl. Electrochem.* **29** (1999) 1409.
11. V. Gurau, F. Barbir and H.T. Liu, *J. Electrochem. Soc.* **147** (1999) 2468.
12. Z.H. Wang, C.Y. Wang and K.S. Chen, *J. Power Sources* **37** (2000) 1151.
13. J. Bear and J.M. Buchlin, 'Modeling and Application of Transport Phenomena in Porous Media' (Kluwer Academic Publishers, Boston, MA, 1991).
14. K.C. Rolle, 'Heat and Mass Transfer' (Prentice Hall, New Jersey, 2000).
15. S.V. Patankar, 'Numerical Heat Transfer and Fluid Flow' (Hemisphere, New York, 1980).
16. J.P. Van Doormaal and G.D. Raithby, *Num. Heat Mass Transfer*, Part A, **7** (1992) 147.
17. J.J. Hwang and D.Y. Lai, *Int. J. Heat Mass Transfer* **41** (1998) 979.
18. D. Natarajan and T.V. Nguyen, *J. Electrochem. Soc.* **148** (2001) 1324.
19. F. Jaouen, G. Lindbergh and G. Sundholmb, *J. Electrochem. Soc.* **149** (2002) 437.
20. G. Murgia, L. Pisani, M. Valentini and B. D'Aguanno, *J. Electrochem. Soc.* **149** (2002) 31.
21. W.K. Lee, S. Shimpalee and J.W. Van Zee, *J. Electrochem. Soc.* **150** (2003) 341.